

# Efficient electrodynamic stripping for 12-inch wafer-scale freestanding ferroelectric oxide membranes

Received: 2 May 2025

Accepted: 11 November 2025

Published online: 23 November 2025

 Check for updates

Hangren Li<sup>1,2,12</sup>, Jie Tu<sup>1,12</sup>, Siyuan Du<sup>1,12</sup>, Guoqiang Xi<sup>1,3,12</sup>, Chen Liu<sup>4,12</sup>, Yue-Wen Fang<sup>5</sup>, Shuai Xu<sup>6</sup>, Jia-Han Zhang<sup>7</sup>, Enqi Sun<sup>8</sup>, Shunli Ouyang<sup>9</sup>, Xudong Liu<sup>1</sup>, Longyuan Shi<sup>1</sup>, Xiuqiao Liu<sup>1</sup>, Dongxing Zheng<sup>4</sup>, Lei Guo<sup>10</sup>, Xixiang Zhang<sup>4</sup>, Kuijuan Jin<sup>6</sup>, Jianjun Tian<sup>1</sup>, Linxing Zhang<sup>1,11</sup> ✉ & Xianran Xing<sup>11</sup> ✉

Developing an efficient and non-destructive stripping method suitable for most fragile freestanding films is essential for developing industrial semiconductor integration and flexible devices. Here, we propose a rapid stripping process of directional electrodynamic decomposition based on the conductive LaNiO<sub>3</sub> sacrificial layer, which can effectively overcome the surface tension during solution penetration. Notably, the release rate of oxide films can be increased to 600 mm<sup>2</sup>/min, which is two orders of magnitude more than that of traditional soaking method, ascribed to the improvement of the adsorption energy and electron transfer by the electric field. The electrodynamic stripping efficiency is not limited by thickness and area size of sacrificial layers and enables non-destructive and scalable fabrication of freestanding films. The crack-free 3-inch freestanding PbZrO<sub>3</sub> epitaxial membrane represents the largest ferroelectric-based membrane achieved to date, which enables its direct integration into flexible piezoelectric sensor array. Intriguingly, a record-breaking 12-inch polycrystalline membrane has been developed to address the requirements of industrial-scale semiconductor manufacturing. The strain-relaxed PbZrO<sub>3</sub> membranes exhibit the hysteresis loop of the antiferroelectric transition to ferroelectric. This electrodynamic approach with conductive sacrificial layer will greatly improve the stripping efficiency of high-quality functional freestanding membranes, thereby promoting their application in wafer-level electronic devices.

Freestanding oxide membrane materials exhibit outstanding physical properties and possess a diverse array of applications, stemming from their independence from the substrate<sup>1–4</sup>. Notably, high-quality freestanding oxide membranes, as small as a single cell<sup>5</sup>, can be created and integrated with various materials to form innovative artificial heterostructures for electronic application<sup>6–11</sup>. The exceptional structural flexibility of freestanding oxide membranes has broadened the

scope for exploring their physical properties, paving the way for the development of functional films such as ferroelectric, ferromagnetic, multiferroic, and superconducting materials<sup>12–14</sup>. The production of freestanding thin films is primarily divided into two categories: chemical and physical techniques<sup>15</sup>. Among these, chemical decomposition stripping stands out for its high throughput and low energy consumption, making it particularly suitable for the industrial

A full list of affiliations appears at the end of the paper. ✉ e-mail: [linxingzhang@ustb.edu.cn](mailto:linxingzhang@ustb.edu.cn); [xing@ustb.edu.cn](mailto:xing@ustb.edu.cn)

development of freestanding films<sup>16,17</sup>. The careful selection of sacrificial layers in chemical decomposition is crucial for the successful application of freestanding oxide membranes. Several materials have been developed to serve as sacrificial layers, which facilitate the separation of functional epitaxial films from the substrates through the chemical decomposition of these layers<sup>18–21</sup>, such as the Sr<sub>3</sub>Al<sub>2</sub>O<sub>6</sub> and Sr<sub>4</sub>Al<sub>2</sub>O<sub>7</sub> water-soluble sacrificial layers<sup>4,22–24</sup>, the SrTiO<sub>3</sub> (STO) and La<sub>0.7</sub>Sr<sub>0.3</sub>MnO<sub>3</sub> acid-soluble sacrificial layer<sup>25,26</sup>.

The chemical decomposition of the sacrificial layer used at present is an immersion method that relies on natural liquid penetration. The decomposition process would generate narrow gaps, typically ranging from nanometers, which are significantly smaller than the micron-scale wetting angle of the decomposition solution. Therefore, due to the action of liquid tension, this natural penetration has a great resistance, similar to the capillary phenomenon<sup>27,28</sup>. Especially, this resistance increases greatly as the thickness of the sacrificial layer decreases, resulting in a decrease in the stripping speed. Furthermore, during the decomposition of the sacrificial layer, the decomposition fluid does not maintain a continuous flow, and the solvent pressure outside the gap remains constant<sup>29</sup>. As decomposition progresses, the contact area between the decomposition fluid and the gap walls increases, leading to heightened friction<sup>30</sup>. Consequently, the decomposition time will increase exponentially with the increase of the area of the freestanding film, which significantly restricts the potential for rapid production in future large-scale industrialization. Therefore, it is urgent to develop a fast-stripping method of chemical decomposition based on the universal sacrificial layer, which would be of significant interest for the sustained progress and prospective applications of freestanding thin film in functional devices.

Here, we introduce a rapid stripping process of directional electrodynamic decomposition (DED) based on the conductive LaNiO<sub>3</sub> (LNO) sacrificial layer, which adeptly navigates the challenges associated with flow limitations and liquid tension within nanoscale gaps. Surprisingly, the release rate has been improved from 5 mm<sup>2</sup>/min of the traditional soaking to 600 mm<sup>2</sup>/min of the DED method, which is a two orders of magnitude improvement, and is not limited by thickness and area size. Meanwhile, the conductive sacrificial layers of LNO perovskite offer 100% atomic matching with a wide range of functional perovskite oxides, ensuring extensive lattice compatibility. Furthermore, the process has improved operability, such as the solvent used for DED is a mild and weak acid, which will not cause damage to the target layer, and the high-quality sacrificial layer can be prepared by low-cost chemical methods due to its stability in atmospheric conditions. This pioneering method establishes a solid foundation for the future industrial deployment of wafer-scale freestanding oxide membranes.

## Results

### Design proposal of DED process based on conductive sacrificial layer

The DED process means that through a specific electric field or device design, the ions in the electrolyte move in a predetermined direction to achieve the decomposition reaction of the sacrificial layer. To ensure the electrical decomposition, the conduction of the sacrificial layer is necessary to ensure the conduction of the circuit. The classical perovskite system LNO has excellent electrical conductivity, which has been widely used as an electrode material. In addition, we chose the LNO system as the sacrificial layer for several important reasons. One is that they are relatively stable in the air and suitable for cost-effective chemical methods, improving operability; Second, their decomposition solution is weak acid, as described below, which will not destroy the target layer, but also provide charge carriers for the solution to conduct electricity; The third is that, due to their perovskite structure, the LNO sacrificial layer can achieve a 100% atomic match with most perovskite functional oxides, establishing a foundation for the fabrication of high-quality freestanding films.

The sacrificial layers of LNO do not react with water, which ensures their stability during preparation in atmospheric conditions. Therefore, we chose the chemical solution deposition (CSD) method to prepare them, benefiting from its simplicity, cost-effectiveness, and precise elemental control. The sacrificial layer was prepared on the single-crystal substrate by the simple sol-gel method of CSD (Supplementary Fig. 1), a technique known for yielding high-quality epitaxial films<sup>31</sup>. Synchrotron-based X-ray diffraction (XRD) patterns demonstrate the epitaxial growth and phase purity of films (Fig. 1a). The presence of satellite peaks, adjacent to the main substrate peak (Inset of Fig. 1a), and X-ray reflectivity (XRR) patterns (Supplementary Fig. 2a) indicate a high degree of crystallinity and surface flatness for the LNO sacrificial layer prepared by CSD<sup>32</sup>. The thickness of the sacrificial layer can be flexibly adjusted by manipulating precursor concentration and process parameters. Synchrotron-based reciprocal space mapping (RSM) around the (103) plane of the substrates reveals the epitaxial growth of LNO on the STO (Fig. 1b). The scanning transmission electron microscopy (STEM) image presents a perfectly atomic-matched interface of the LNO film and the STO substrate, further illustrating the epitaxial growth of LNO (Fig. 1c). The LNO sacrificial layer can also be epitaxial prepared on different single-crystal substrates and different orientation substrates (Supplementary Fig. 2b and 2c). The chemical epitaxial growth of LNO perovskite sacrificial layer offers the possibility for industrial applications.

By connecting the sacrificial layer to the positive electrode of a power supply, with a graphite rod or metal electrode serving as the negative electrode, both electrodes are immersed in a mildly acidic electrolyte, such as 10% concentration of acetic acid (Fig. 1d). The current will preferentially flow from the acetic acid electrolyte to the sacrificial layer as they are both conductive. Meanwhile, under the action of electric field, the electrolyte obtains the power to overcome the interface friction, and can move rapidly and directionally, and decompose the sacrificial layer quickly, which effectively improve the characteristics of the solid-liquid interface and overcome the resistance caused by surface tension (Fig. 1e). The LaNiO<sub>3</sub>(s) + 6CH<sub>3</sub>COOH(aq) → La(CH<sub>3</sub>COO)<sub>3</sub>(s or aq) + Ni(CH<sub>3</sub>COO)<sub>3</sub>(s or aq) + 3H<sub>2</sub>O(l) chemical reactions will take place, subsequently, the salt substances will re-dissolve in the solution. The electric field only accelerates the reaction rate without generating new redox reactions. The decomposition of water into hydrogen and oxygen will act as an additional reaction. There is a side reaction in the positive electrode, which will produce hydrogen ions, conducive to accelerating the decomposition of the sacrificial layer. And there are no solid by-products.

Before DED, through exploration, we found that the weak acid can dissolve LNO, and a slow spontaneous decomposition process of LaNiO<sub>3</sub>(s) + 6H<sup>+</sup>(aq) → La<sup>3+</sup>(aq) + Ni<sup>3+</sup>(aq) + 3H<sub>2</sub>O(l) chemical reactions will act during the immersion process. Although the decomposition rate of medium or strong acids is faster, to ensure that the target layer is not destroyed, we choose the weak acid of acetic acid as the solvent. When the concentration of acetic acid reaches 10%, the best immersion decomposition rates can be obtained, which is equivalent to the concentration of edible vinegar in life. To analyze the decomposition process of the sacrificial layer, we used ultraviolet-visible (UV-Vis) spectroscopy (Supplementary Fig. 3). The decomposition rate was evaluated by monitoring the intensity of the characteristic absorption peak of the sacrificial layer. The decomposition curve of UV-Vis spectroscopy indicates the DED method shows an obviously faster trend of decreasing intensity (Fig. 1f). The LNO (100 nm)/STO sample by DED takes only 15 seconds to completely decompose, while the soaking method does take more than 30 minutes, which is an improvement of two orders of magnitude. The decomposition of the LNO/STO sample is further corroborated by macroscopic optical imaging (Fig. 1g). It can be intuitively seen that after 15 seconds of electrical decomposition, the sample changed from all black to completely transparent of the

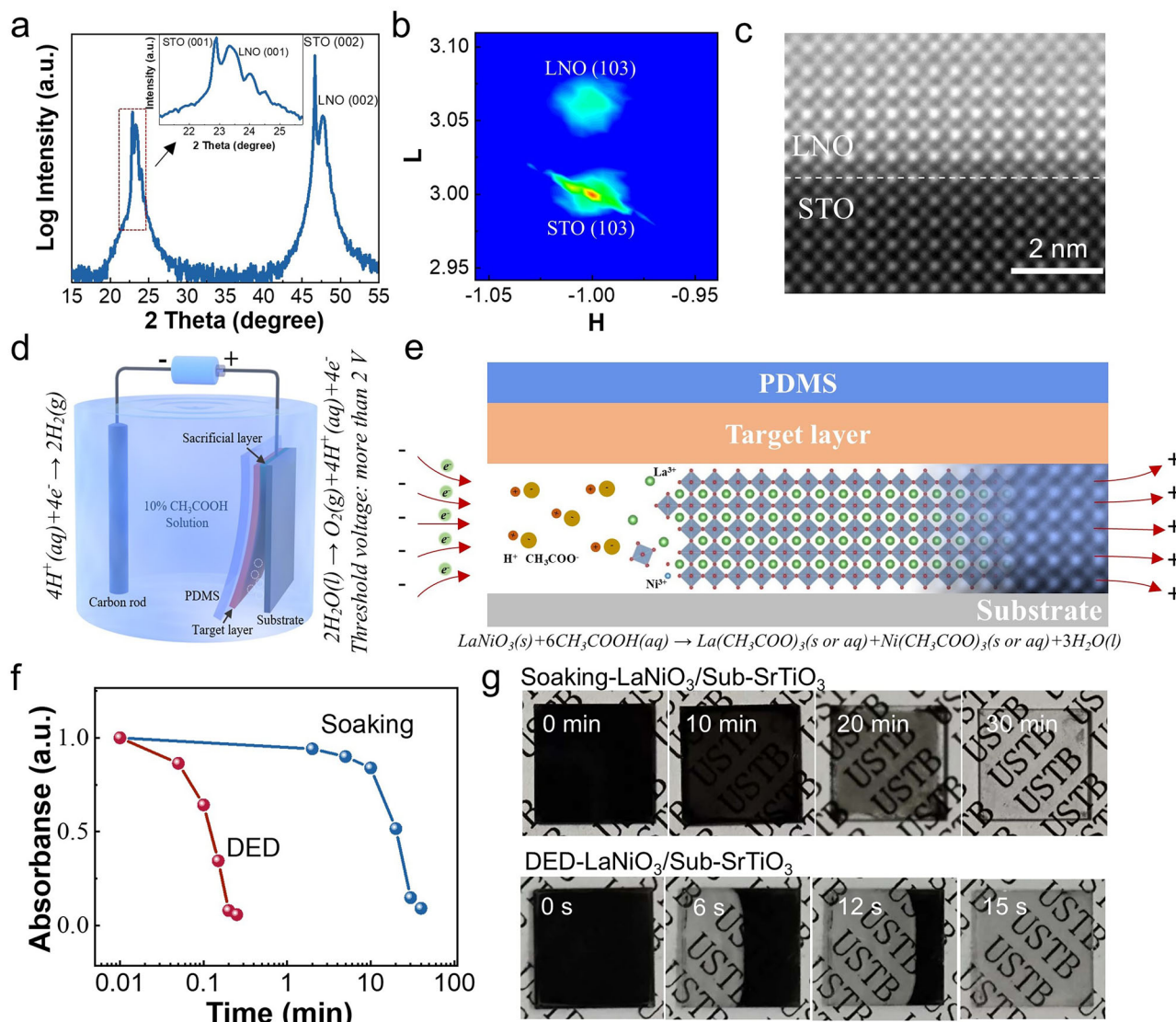


**Fig. 1 | Conductive sacrificial layers and design proposal of DED process.**

**a** Synchrotron-based XRD patterns of LNO sacrificial layers on (001) oriented STO substrates. a.u., arbitrary units after logarithmic processing. The inset shows the (001) peaks with the satellite peaks, indicating the high-quality film. **b** Synchrotron-based X-ray RSMs of sacrificial layers around STO (103) diffraction regions. L, crystal index of (00L); H, crystal index of (H00). **c** STEM images of LNO film grown on the STO substrate, indicating the high-quality epitaxial relationship. **d** Schematic

illustration of the DED process of the LNO sacrificial layer. The DED setup utilized in this study comprises a power supply and a carbon electrode paired with a positive PDMS/film/LNO/substrate assembly. **e** Schematic illustration of the DED mechanism for the LNO sacrificial layer. **f** Absorption intensity at 30 nm is dependent on the time for the LNO sacrificial layer using DED and conventional soaking methods. **g** Photographs of sacrificial layers decomposition via DED and conventional soaking approaches. The size of the STO substrate is 10 × 10 mm<sup>2</sup>.

STO single-crystal substrate, indicating that the sacrificial layer was completely decomposed. This time for the soaking method is 30 minutes, consistent with the UV-Vis spectroscopy results. Interestingly, the DED process also shows the controllable direction of decomposition, which is caused by the orientation of the current, while the soaking method presents the state of overall decomposition from the surface because there is no film cover. The directional nature of this electrodynamic method will make possible the diversity of stripping (Supplementary Fig. 4). The directional decomposition process of the sacrificial layer has a uniform current density, enabling the freestanding preparation of thin films with different orientations.

#### Controllability and ultra-fast release rate of the DED process

In addition to the above controlled electrodynamic direction, the present DED has many controllable parameters to adjust the decomposition rate of the sacrificial layer, such as the electrodynamic voltage, the thickness of the sacrificial layer, and the substrate size. With

the increase of electrodynamic voltage from 0.1V to 25V, the decomposition time of LNO sacrificial layer LNO (10 × 10 × 0.5 mm<sup>3</sup>) is gradually shortened, and only 15 seconds of decomposition need to be completed at 25 V (Fig. 2a). Our findings reveal a positive correlation between the magnitude of the applied voltage and the decomposition rate of the sacrificial layer. This observation underscores the facilitative role of the electric field and holds significant potential for enabling the future efficient fabrication of large-scale freestanding oxide membranes.

In the traditional soaking method, with the increase of the sacrificial layer area or the decrease of thickness, the rate shows an obvious downward trend, which is due to the existence of surface tension. We further performed decomposition experiments covering the target layer of PbZrO<sub>3</sub> (PZO) films. Intriguingly, the DED method showed the opposite trend, and the thinner the thickness, the faster the decomposition rate in the DED approach (Fig. 2b). In the stripping of the target layer, the rate of the traditional soaking method is 0.27 mm<sup>2</sup>/min

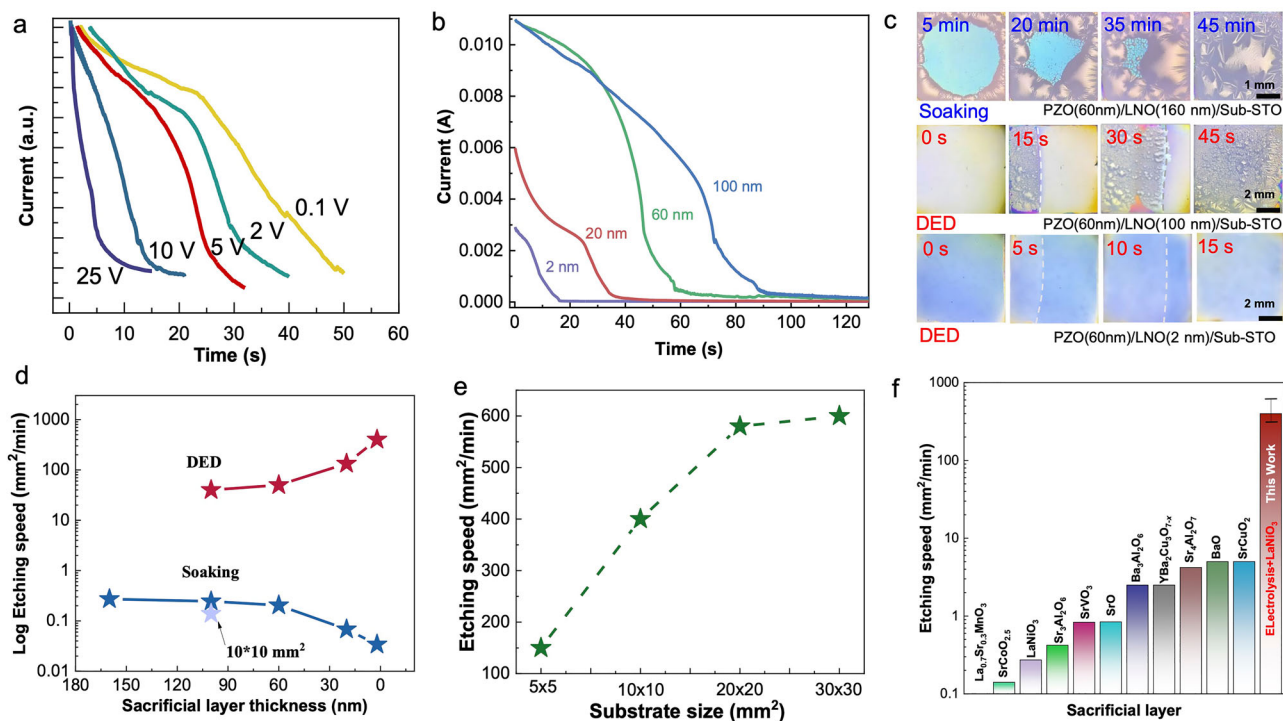


**Fig. 2 | Controllability and ultra-fast release of the DED process.** **a** Current-time curves for DED decomposition of the 100 nm LNO/STO ( $10 \times 10 \text{ mm}^2$ ) sample at various voltages. **b** Current-time curves for DED of the PZO/LNO/STO ( $10 \times 10 \text{ mm}^2$ ) samples at various thickness of LNO. **c** Optical micrographs of sacrificial layers decomposition via DED and conventional soaking approaches, covering the target layer of PZO films. **d** Stripping rate of DED ( $10 \times 10 \text{ mm}^2$ ) and conventional soaking

( $5 \times 5 \text{ mm}^2$ ) processes at various sacrificial layer thicknesses. The light blue five-pointed star shows the rate of large areas ( $10 \times 10 \text{ mm}^2$ ) in the soaking method, showing the reduced rate. **e** Stripping rate of DED at different sample area sizes. **f** Statistics of stripping rate of the traditional soaking method for various sacrificial layers and the DED method.

for PZO (60 nm)/LNO (160 nm)/STO sample (Fig. 2c), which is close to that of  $\text{Sr}_3\text{Al}_2\text{O}_7$ <sup>25</sup>. The rate of the DED method is greatly improved to  $133 \text{ mm}^2/\text{min}$  for the PZO (60 nm)/LNO (100 nm)/STO sample. We found that immersion is a natural way of decomposition from all sides to the center, while DED is oriented, as described above. Notably, when the sacrificial layer thickness is reduced to 2 nm, the DED rate reaches a higher value of  $400 \text{ mm}^2/\text{min}$  for PZO (60 nm)/LNO (2 nm)/STO sample (Fig. 2c and Supplementary Fig. 5). The strain state of the sacrificial film can affect the rate of electrical decomposition, and the change of strain caused by the reduction of sacrificial layer thickness should promote the increase of decomposition rate, which is based on the premise of overcoming the capillary effect caused by the surface tension. Meanwhile, we find that with the reduction of the thickness of the sacrificial layer, the target layer of PZO films presents crack-free and wrinkle-free at the millimeter size (Supplementary Fig. 6). When the thickness of the sacrifice layer is reduced from 160 nm to 2 nm, the stripping rate of the soaking method is reduced from  $0.27 \text{ mm}^2/\text{min}$  to  $0.034 \text{ mm}^2/\text{min}$  (Fig. 2d and Supplementary Fig. 7), indicating the increasing surface tension. Unfortunately, the wrinkles can't be removed in the traditional soaking method.

When the area of the sample is increased from  $25 \text{ mm}^2$  to  $100 \text{ mm}^2$ , the stripping rate of the soaking method decreases from  $0.25 \text{ mm}^2/\text{min}$  to  $0.14 \text{ mm}^2/\text{min}$  (Fig. 2d and Supplementary Fig. 8). Notably, we found that the rate of the DED method increased with the increase of the area, and tends to be constant when it approaches  $30 \times 30 \text{ mm}^2$ , reaching a maximum of  $600 \text{ mm}^2/\text{min}$  (Fig. 2e). As the sacrificial layer's area and side length increase, its cross-sectional area also grows. A larger cross-sectional area provides more active sites for the DED reaction, which can potentially enhance the reaction rate. However, if the cross-sectional area becomes excessively large, the current density distribution may become uneven, thereby limiting the overall improvement in the decomposition rate. We sorted out the rate of the traditional

soaking method for various sacrificial layers reported to date, basically belonging to the single-digit or lower rate (Fig. 2f and Supplementary Table 1). The highest of them are  $\text{Sr}_4\text{Al}_2\text{O}_7$ , BaO, and  $\text{SrCuO}_2$ , with only 4–5  $\text{mm}^2/\text{min}$ . However, the present rate of the DED process is two orders of magnitude higher than the maximum value of the traditional method, indicating a significantly more efficient. This enables the rapid fabrication of high-quality, wafer-scale, freestanding oxide single-crystal films, from which we stripped the complete PZO freestanding film with a diameter of several inches, as presented below.

### Mechanism of rapid stripping by the DED process

Density functional theory calculations indicate that the electric field enhances the affinity of acetate molecules for La atoms at the LNO interface, resulting in reduced interfacial adsorption energy from 0.79 eV without the electric field to  $-0.21 \text{ eV}$  with the electric field (Fig. 3a). Through the differential density charge maps with or without electric field, it can be found that the electrons around La are decreasing, while the electrons of oxygen in the acetic acid free radical are increasing (Fig. 3b). The Bader charge difference between with and without an electric of La is 0.0055 electrons, while that of O in acetic acid is much higher, 0.0178 electrons (Fig. 3c). According to the Bader charge, LNO transfers 0.8270 electrons to the acetic acid radical when there is no electric field, and 0.8712 electrons to the acetic acid radical when there is an electric field. Differential density charge maps and Bader charge analysis reveal that the electric field increases the transfer of electrons from La atoms to the acetate molecule. This suggests that the electric field can facilitate the exchange between LNO and acid ions in the solvent, thereby accelerating the decomposition process. In addition, these findings supported the electrocatalysis of electric field acceleration.

Molecular dynamics simulations demonstrate that the solution group under an electric field is more compressed than the solution

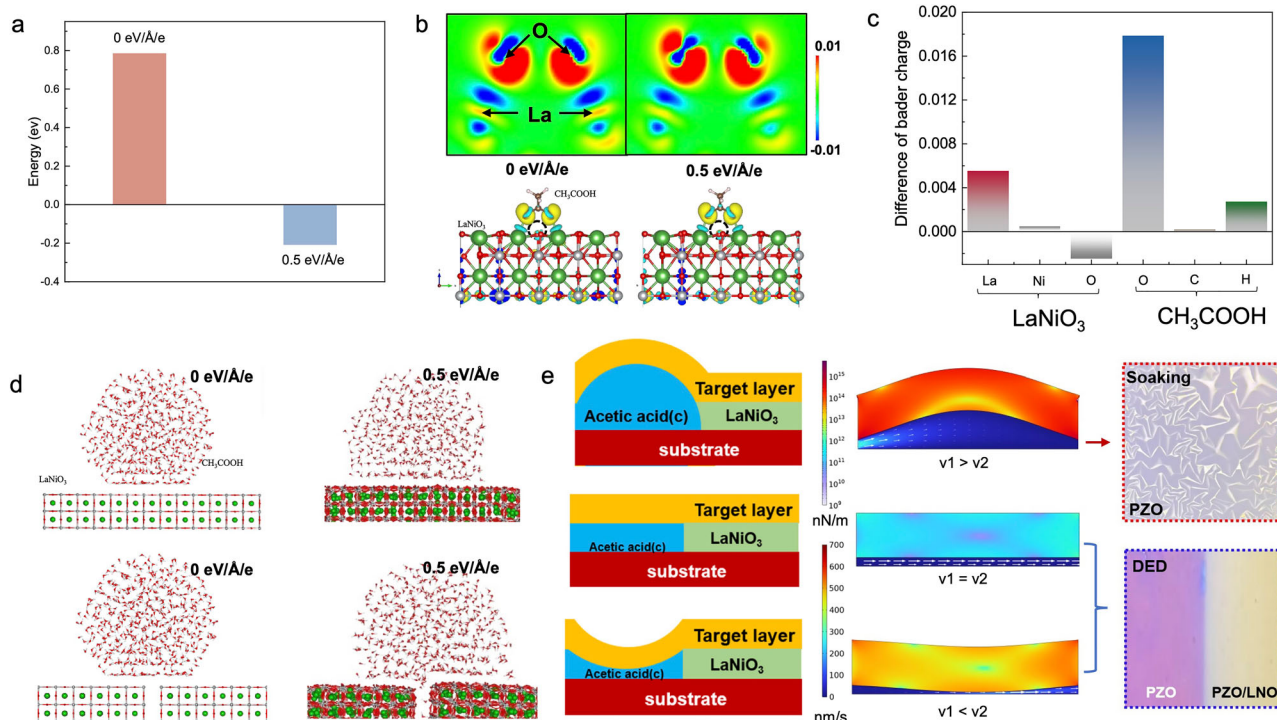


**Fig. 3 | Theoretical calculation and simulation of DED process.** **a** Interfacial adsorption energy of the acetate molecules and the LNO with and without an electric field (0.5 eV/Å/e). **b** Density functional theory calculations elucidating the electron transfer dynamics of LNO and CH<sub>3</sub>COOH. **c** Bader charge difference between with and without an electric field (0.5 eV/Å/e). **d** Molecular dynamics simulations assessing the interfacial affinity between the CH<sub>3</sub>COOH droplet and LNO in the presence and absence of an electric field. The upper part of the figure

refers to the absence of gaps in the sacrifice layer, and the lower part refers to the presence of gaps in the sacrifice layer, which may be generated during the decomposition process. **e** Schematic diagram and a finite element simulation diagram of soaking decomposition and the DED method. The  $v_1$  and  $v_2$  are the diffusion velocity and the decomposition velocity, respectively. The upper part is the case of soaking decomposition, and the middle and lower parts are the case of the DED process.

group without an electric field (Fig. 3d). This compression can be attributed to several factors influenced by the presence of the electric field. Firstly, the electric field induces a dipole moment in the molecules of the solution, causing them to align in the direction of the field. This alignment enhances the intermolecular interactions, particularly the electrostatic attractions between polar molecules, leading to a more compact structure. Secondly, the electric field can also influence the distribution of ions within the solution. Positively charged ions tend to move towards the negative electrode, while negatively charged ions move towards the positive electrode. This movement and redistribution of ions can create a more ordered and compressed arrangement compared to the random distribution observed in the absence of an electric field. Moreover, the increased compression under an electric field can have significant implications for various properties of the solution, such as its viscosity, conductivity, and diffusion behavior. For instance, the enhanced intermolecular interactions and ion movement can lead to higher viscosity and altered diffusion rates, which are critical factors in many chemical and biological processes. This indicates that the electric field provides an additional driving force for the migration of the solution group to the LNO surface. Concurrently, molecular dynamics also show that electric fields can rapidly and directionally penetrate solution groups within narrow gaps, which confirms that the electric field can overcome the influence of surface tension. These findings provide a theoretical foundation for the feasibility of ultra-fast DED process of sacrificial layers.

To elucidate the mechanism behind the formation of a flat and crack-free film via electrical stripping, finite element simulation analysis was conducted, as illustrated in Fig. 3e. The simulation reveals that the decomposition rate and solution flow dynamics play crucial roles in determining the film's surface morphology. In the soaking

scenario, the decomposition rate is relatively slow, allowing the solution to continuously infiltrate the gap between layers ( $v_1 > v_2$ ). This excess inflow causes the film to bulge, subsequently leading to the formation of folds. Conversely, in the case of DED, the decomposition rate is significantly faster. The inflow rate of the solution is either less than or equal to the decomposition rate, meaning that the solution entering the gap can quickly flow out. This rapid egress prevents the film from bulging and thus ensures a smooth and flat surface. Additionally, when the sacrificial layer is thinner, the electrical decomposition rate increases, further enhancing the film's flatness. Another contributing factor is that a thinner sacrificial layer subjects the target layer to less strain change, reducing the likelihood of collapse (Supplementary Fig. 9). These findings collectively explain why electrical stripping can produce a flat and crack-free film.

### Microstructure and physical properties of freestanding oxide membranes

Intriguingly, LNO exhibits a high degree of lattice matching tolerance, ranging from 3.69 Å to 4.21 Å. We selected the orthorhombic PZO system with antiferroelectric, the rhombohedral BiFeO<sub>3</sub> (BFO) system with ferroelectric, and the cubic STO system with dielectric characteristics as the target layers (Supplementary Fig. 10). Their lattice constants, according to the pseudo-cubic structure, are approximately 4.21 Å, 3.95 Å, and 3.91 Å, respectively. For the stripping of the STO target layer, LaAlO<sub>3</sub> (LAO) with a lattice constant of 3.79 Å was employed as the growth substrate, demonstrating that LNO is compatible with LAO and can be epitaxially grown with high quality. Additionally, we can also successfully strip the undamaged LAO and YMnO<sub>3</sub> (YMO) ( $a_{\text{pseudocubic}} = 3.69$  Å) as the target layer (Supplementary Fig. 11). This underscores LNO's extensive lattice matching capability, spanning from 3.69 Å to 4.21 Å.

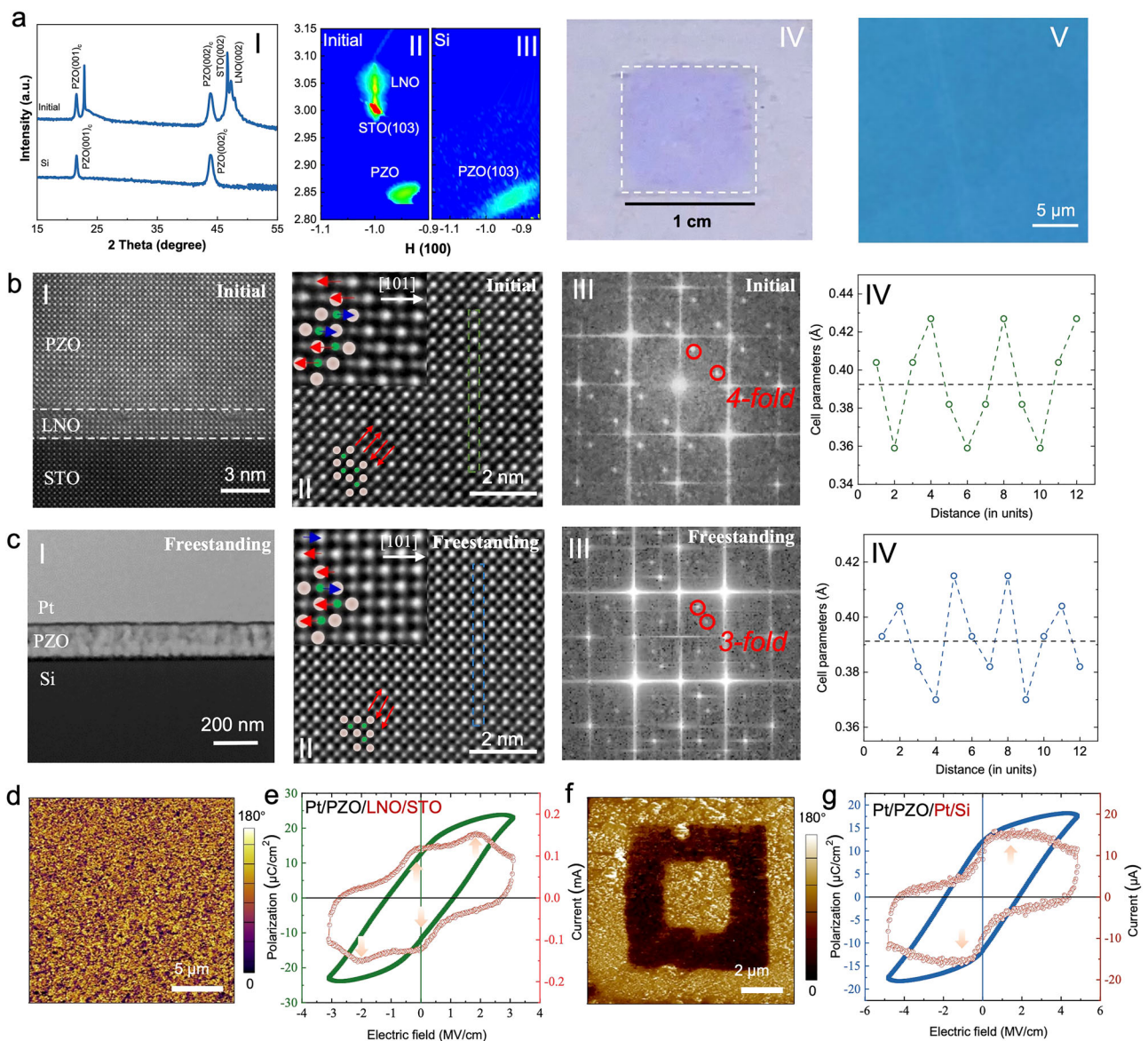


**Fig. 4 | Structure and physical properties of PZO freestanding oxide membranes.** **a** The structure and morphology of PZO epitaxial films before and after stripping. **I** XRD patterns of PZO films before and after stripping. Reciprocal space mapping (RSM) studies of PZO films around (103) peak **II** before and **III** after releasing from the substrate. **IV–VI** Microphotographs of PZO freestanding films at

different magnifications, displaying a significant uncracked and flat morphology. STEM images and FFT of **b** as-grown PZO thin film and **c** freestanding PZO membrane. Phase images of PFM for **d** as-grown PZO thin film and **f** freestanding PZO membrane. Ferroelectric hysteresis loops and switching current curves of **e** as-grown PZO thin film and **g** freestanding PZO membrane.

Both the sacrificial layer and the target layer were deposited using the CSD method, except for BFO, which was deposited by radio-frequency magnetron sputtering. The target layers grown on the LNO sacrificial layer exhibited exclusive (00 $l$ ) peaks, signifying their epitaxial orientation as confirmed by XRD and RSM scans (Figs. 4a–I, 4a–II and Supplementary Fig. 12). Freestanding membranes were successfully stripped and transferred onto Si substrates, retaining their original epitaxial properties (Fig. 4a–III and Supplementary Fig. 13). A comparative analysis of synchrotron-based XRD and RSM before and after the stripping process indicates the viability of our DED method for fabricating freestanding single-crystal thin films. The RSM of the stripped sample revealed minor structural relaxation, such as an increase in the out-of-plane lattice constant for PZO and a decrease for BFO, which could potentially induce structural distortion and impact performance. The PZO freestanding membrane exhibits flat and unbroken (Figs. 4a–IV, 4a–V), and the thickness can be controlled (Supplementary Fig. 14). Similarly, the BFO and STO freestanding

membranes also exhibit relatively flat without broken (Supplementary Fig. 12). All freestanding films exhibit minimal damage, and it is possible to consistently obtain relatively intact films. This result underscores the high compatibility of the DED process and the selected sacrificial layer system. The stripping of the target layer is achievable so long as its resistance exceeds that of the LNO sacrificial layer.

High-angle annular dark-field scanning transmission electron microscopy (HAADF-STEM) analysis of various perovskite films revealed the single-crystal nature of the films both before and after the stripping process, corroborating the findings from XRD studies (Fig. 4b, c). The observation of multiple interfacial lattices with good matching further validates the high compatibility of LNO as a sacrificial layer, as evidenced by the well-aligned interfaces such as STO/LNO, LNO/PZO (Fig. 4b–I), LNO/BFO (Supplementary Fig. 15), and LAO/LNO (Supplementary Fig. 16)<sup>33</sup>. We have successfully fabricated freestanding films with various phase structures through LNO sacrificial layers spanning a range of thicknesses from 2 to 60 nm. For instance,

PZO films were achieved with a 2 nm LNO layer, BFO thin films with a 16 nm LNO layer, and STO thin films with a 60 nm LNO layer. This highlights the high adaptability of the fabrication process through varying sacrificial layer thicknesses. The PZO film transferred to the Si substrate exhibits an exceptional degree of flatness (Fig. 4c–I). The wide range of STEM images indicates the high-quality single-crystal nature of the PZO film both before and after stripping (Figs. 4b–II, 4c–II). By Fast Fourier Transform (FFT), we identified the presence of both pseudo-cubic regions (not shown) and orthorhombic regions (Fig. 4b–III) within initial PZO thin films<sup>34</sup>. Notably, a transformation is observed in the orthorhombic structure regions from a fourfold modulation period before stripping to a threefold modulation period after stripping (Fig. 4c–III). This alteration may arise from structural distortion following strain release, a finding that aligns with the results of RSM and geometric phase analysis (GPA) (Supplementary Fig. 17). We calculated the out-of-plane lattice constants of these two regions and found that the initial PZO film has a period of 4 pseudo-cubic cells while the stripped film has a period of 3 pseudo-cubic cells, which further confirmed the structural phase transition (Figs. 4b–IV, 4c–IV). Such structural reconfiguration suggests a phase transition from an antiferroelectric to a ferroelectric state<sup>35</sup>, which was further confirmed by subsequent property testing.

No discernible switching behavior is observed in the domain writing process of piezoresponse force microscopy (PFM) (Fig. 4d), which may be attributed to the antiferroelectricity of the as-grown PZO film depending on its inherent characteristic. In contrast, the freestanding PZO film exhibits distinct 180° domain switching (Fig. 4f)<sup>36</sup>, indicative of a transition towards ferroelectric properties<sup>37</sup>. For the as-grown film, we used Pt/PZO/LNO/STO structure for ferroelectric testing of the hysteresis loop (Fig. 4e). The presence of four switching peaks in the switching current curve confirms the antiferroelectric property of the as-grown film<sup>38,39</sup>. Strikingly, a standard hysteresis loop was obtained for the stripped freestanding PZO membrane using the Pt/PZO/Pt/Si structure (Fig. 4g). Typically, demonstrating a macroscopic hysteresis loop for a freestanding film is challenging due to the risk of film damage. The hysteresis loop of the PZO freestanding membrane indicates the high quality of the stripped film. It can be found from the switching current curve that there is a gradual transition to two switching peaks, which further confirms the ferroelectric transition caused by the structural transformation after strain release. This finding aligns closely with the results obtained from TEM and PFM analyses discussed earlier. Furthermore, the BFO freestanding film exhibits enhanced ferroelectric properties and structural transformation after transfer, and the STO film shows high flatness, crystallinity, and excellent dielectric performance (Supplementary Figs. 18 and 19).

### Large-scale freestanding oxide membranes and devices

The DED method has demonstrated exceptional capability in large-area stripping of freestanding oxide films, showcasing its potential for wafer-level semiconductor applications. A single crystal LAO with a diameter of 3 inches was selected as the substrate for the epitaxial growth film (Fig. 5a). LNO can grow epitaxial on the LAO substrate, as described above. We achieved uniform growth of the LNO buffer layer with complete surface coverage, as evidenced by its homogeneous black coloration across the entire substrate. Subsequent deposition of the PZO target layer via chemical solution processing yielded a macroscopically smooth and defect-free surface, highlighting the scalability of this approach. Notably, the fast DED method enabled clean separation of the PZO layer without residual sacrificial/target layers on the LAO substrate. Such a substrate can be repeated dozens of times (Supplementary Fig. 20), which is the critical advance for industrial productivity. This phenomenon is not limited to LAO substrates, and STO substrates also exhibit the same repeatability. The 3-inch freestanding PZO film exhibited remarkable uniformity and mechanical robustness with no observable cracks or delamination (Fig. 5b and

Supplementary Fig. 21). XRD analysis of six representative regions confirmed consistent crystallographic structure with the same PZO peaks (Fig. 5c), indicating that the stripping process did not cause the collapse of films and lead to inconsistent orientation.

The freestanding films were utilized to fabricate piezoelectric sensors designed for detecting flexible deformation and converting it into electrical signals. As depicted in Fig. 5d, a 4 × 5 interdigital electrode array was meticulously prepared on the film surface. When the sensor devices were attached to a human arm, each device in the array generated a distinct piezoelectric signal (Fig. 5e and Supplementary Fig. 22), varying based on the degree of mechanical deformation experienced. For instance, the middle area of the array produced a robust 24 mV signal, while the edge area generated a significantly weaker 5 mV signal. These values are superior to the piezoelectric signal of about 4.29 mV/% shown in the polyvinylidene fluoride<sup>40</sup>. This discrepancy is directly related to the curvature imposed on different regions of the film by the arm. The middle region, subjected to greater curvature, exhibited a stronger piezoelectric response, whereas the edge region, with less curvature, produced a weaker signal. To further investigate this relationship, we collected data correlating the bending degree with the corresponding piezoelectric signal (Supplementary Fig. 23). The results revealed a strong positive correlation between the two (Supplementary Fig. 24). The above results are also confirmed by local piezoelectric signals (Supplementary Fig. 25). Although the piezoelectric properties of the films are limited by the maximum displacement and size effect<sup>41,42</sup>, the piezoelectric responses of freestanding PZO films of different thicknesses have been confirmed by PFM (Supplementary Fig. 26)<sup>43</sup>. This finding underscores the potential of our large-area freestanding films as highly sensitive and adaptable materials for flexible electronic devices, particularly in applications requiring precise detection of mechanical deformation.

To meet the demands of the large-scale semiconductor industry, we undertook the challenge of fabricating a freestanding film with a diameter of 12 inches. Given that perovskite single-crystal substrates are typically not available in such large sizes, we opted for silicon as the substrate to grow polycrystalline films. During the deposition process of the sacrificial layer (LNO) and the target layer (PZO), the surface exhibited specular reflection (Fig. 5f), which indicated that the deposited films were highly uniform flat, and free of pinholes. Structural analysis shows that both LNO and PZO films exhibit high (00 l) preferred orientation, indicating excellent crystallinity (Supplementary Figs. 27a–c). Utilizing the fast DED stripping method, we successfully stripped the 12-inch PZO freestanding film from the substrate. The freestanding film was remarkably intact and flat, although minor bubbles were observed. This may be attributed to the uneven PDMS paste process, which could be removed in the further optimized process. The 12-inch freestanding PZO film on PDMS also presented the preferred orientation structure and high crystallinity, displaying a polycrystalline state and significant uncracked morphology in large area (Supplementary Fig. 27d). The XRD results from 9 random areas indicate that the freestanding film have the uniformity and homogeneity, as their diffraction intensities are comparable (Supplementary Fig. 28). The electrical property (leakage current) of the 12-inch freestanding PZO film also remains at the magnitude of about 10<sup>2</sup> μA/cm<sup>2</sup> of the value before stripping (Supplementary Fig. 29). The successful creation of a 12-inch PZO freestanding film represents a significant milestone, as it is currently the largest freestanding oxide film ever produced. This achievement underscores the potential of the fast DED method to revolutionize the industrial application of freestanding oxide films, paving the way for their integration into advanced electronic devices and flexible technologies.

### Discussion

The universal and efficient stripping process of DED based on the conductive LNO sacrificial layer exhibits significant potential in future

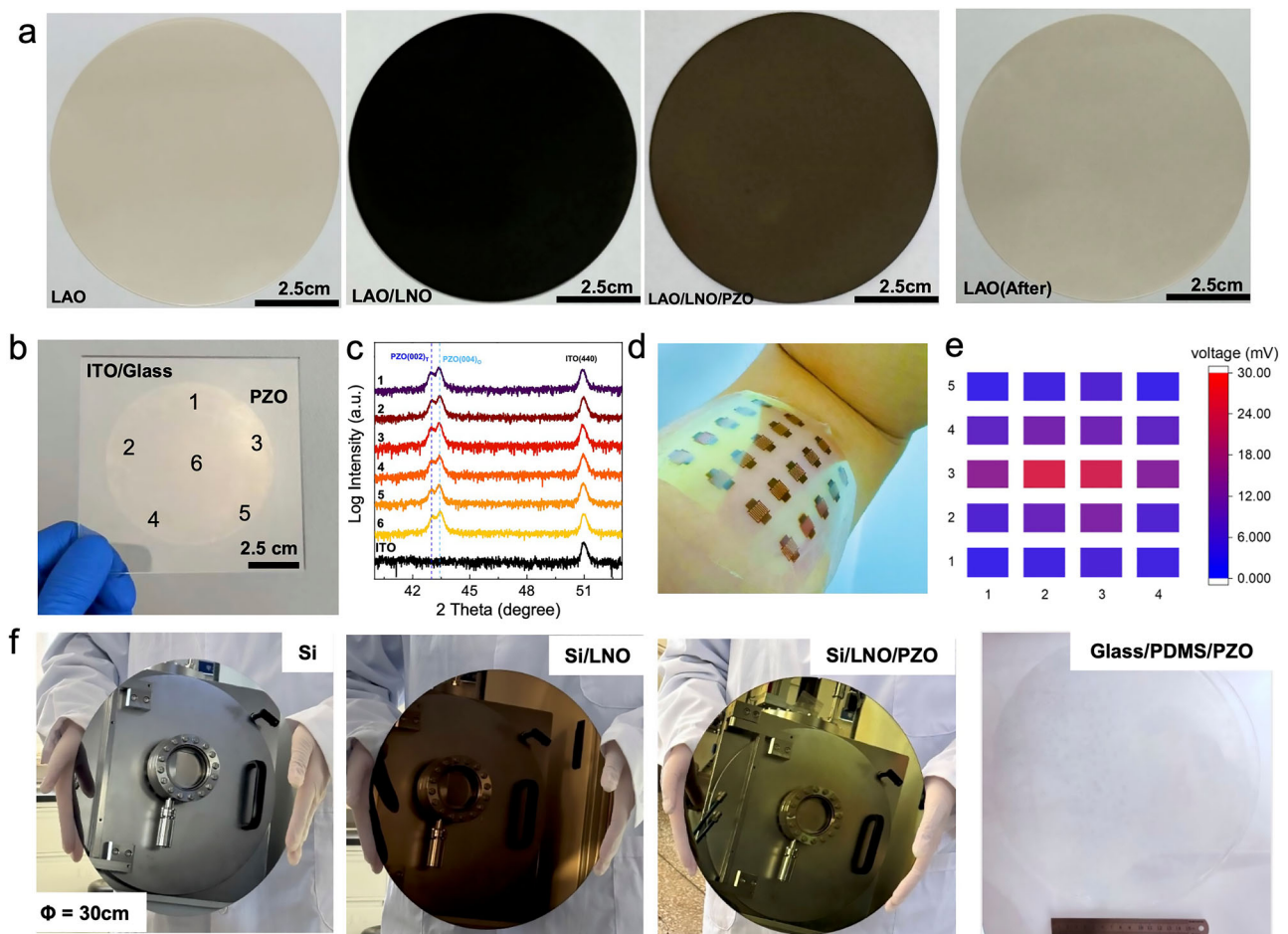


**Fig. 5 | Preparation of large-scale freestanding oxide films and devices.** **a** Optical photos of the 3-inch sample preparation process. **b** Optical photo of the complete 3-inch freestanding PZO film. **c** XRD patterns of different regions in Fig. 5b. The minor peak splitting of PZO suggested strain-induced phase coexistence

originating from the LAO substrate during processing. **d** Array of piezoelectric sensors attached to the arm. **e** Electrical signals of the piezoelectric sensor array in Fig. 5d. **f** Optical photos of the 12-inch sample preparation process and optical photo of the complete 12-inch freestanding PZO film.

large-scale industrialization, leveraging its numerous advantageous properties. Primarily, compared with the traditional soaking method, the rate of the DED stripping method is a qualitative leap, increasing by two orders of magnitude, and is not limited by the thickness and area size of the sacrificial layer, providing a reliable guarantee for large-area stripping. Secondly, the DED stripping method has high controllability; for example, a variety of target layers and diversified stripping modes can be obtained by controlling the voltage value and current direction, respectively. The most critical is that the application of an electric field not only provides the decomposition fluid with the power to overcome the interface friction, but also reduces the tension exerted by the decomposition fluid on the film, which is conducive to obtaining high-quality flat freestanding films. Thirdly, the present LNO sacrificial layer exhibits compatibility with the growth of most perovskite oxides with lattice constants ranging from 3.69 to 4.21 Å, achieving 100% atomic matching. The water insolubility of the present sacrificial layer, as depicted in Supplementary Fig. 30, endows it with enhanced stability, rendering it an ideal candidate for the preparation of target layers via diverse methodologies, especially low-cost chemistry methods. Owing to these attributes, the DED of LNO sacrificial layer offers a versatile and pragmatic strategy for the expeditious fabrication of large-area, crack-free freestanding oxide films, which holds promise for substantially broadening the applicability of freestanding oxide films in emerging, cost-effective, and adaptable device technologies.

## Methods

### Preparation of sacrificial and target films

**LaNiO<sub>3</sub>.** The required amount of Lanthanum nitrate hexahydrate (La(NO<sub>3</sub>)<sub>3</sub>·6H<sub>2</sub>O, aladdin, 99%), Nickel(II) acetate tetrahydrate (NiC<sub>4</sub>H<sub>6</sub>O<sub>4</sub>·4H<sub>2</sub>O, aladdin, 99.9%) is dissolved in 2-Methoxyethanol (C<sub>3</sub>H<sub>8</sub>O<sub>2</sub>, aladdin, 99.5%). Then, the mixed solvent was heated and stirred on a 75 °C hot platform for 2 hours to obtain a transparent precursor solution. Finally, the solvent is left to stand at room temperature for filtration.

The precursor solution is spin-coated on a 10 × 10 mm<sup>2</sup> STO or LAO substrate and rotated at a high speed of 5000 rpm for 30 seconds. On the hot table, the water in the film was removed by heating at 120 °C for 3 minutes, and the organic solvent was removed by heating at 350 °C for 10 minutes. Subsequently, the LNO sample was subjected to annealing in a rapid annealing furnace 650 °C–750 °C for approximately 5 minutes.

**PbZrO<sub>3</sub>.** The required amount of Lead nitrate (Pb(NO<sub>3</sub>)<sub>2</sub>, aladdin, 99.999%) and Zirconium nitrate pentahydrate (Zr(NO<sub>3</sub>)<sub>4</sub>·5H<sub>2</sub>O, aladdin, 99.9%) is dissolved in 2-Methoxyethanol (C<sub>3</sub>H<sub>8</sub>O<sub>2</sub>, aladdin, 99.5%). There was 10% too much lead. Then, the mixed solvent was heated and stirred on a 75 °C hot platform for 2 hours to obtain a transparent precursor solution. Finally, the solvent is left to stand at room temperature for filtration.

The precursor solution is spin-coated on a  $10 \times 10 \text{ mm}^2$  LNO/STO or LNO/LAO substrate and rotated at a high speed of 5000 rpm for 30 seconds. On the hot table, the water in the film was removed by heating at  $120 \text{ }^\circ\text{C}$  for 3 minutes, and the organic solvent was removed by heating at  $350 \text{ }^\circ\text{C}$  for 10 minutes. Subsequently, the PZO sample was subjected to annealing in a hostler furnace  $700 \text{ }^\circ\text{C}$  for approximately 30 minutes.

**SrTiO<sub>3</sub>.** The required amount of Strontium acetate ( $\text{C}_4\text{H}_6\text{O}_4\text{Sr}$ , Mackun, 99%) and Titanium (IV) oxide acetylacetonate ( $\text{C}_{10}\text{H}_{14}\text{O}_5\text{Ti}$ , Aladdin, 98%) is dissolved in acetic acid, then 2, 4-pentanedione is added. A solution with a metal ion concentration of 0.1 mol/L is obtained, in which the ratio of acetic acid to 2, 4-pentanedione is 3:2. Finally, the mixed solvent was heated on a hot table at  $75 \text{ }^\circ\text{C}$  for 2 hours to obtain a transparent precursor solution.

The precursor solution is spin-coated on a  $10 \times 10 \text{ mm}^2$  LNO/LAO substrate and rotated at a high speed of 5000 rpm for 30 seconds. On the hot table, the water in the film was removed by heating at  $120 \text{ }^\circ\text{C}$  for 3 minutes, and the organic solvent was removed by heating at  $350 \text{ }^\circ\text{C}$  for 10 minutes. Subsequently, the STO sample was subjected to annealing in a hostler furnace  $900 \text{ }^\circ\text{C}$  for approximately 30 minutes.

**LaAlO<sub>3</sub>.** The required amount of Lanthanum nitrate hexahydrate ( $\text{La}(\text{NO}_3)_3 \cdot 6\text{H}_2\text{O}$ , aladdin, 99%) and Aluminum triacetylacetonate ( $\text{C}_{15}\text{H}_{21}\text{O}_6\text{Al}$ , aladdin, 99.999%) is dissolved in acetic acid, then 2, 4-pentanedione is added. A solution with a metal ion concentration of 0.1 mol/L is obtained, in which the ratio of acetic acid to 2, 4-pentanedione is 3:2. Finally, the mixed solvent was heated on a hot table at  $75 \text{ }^\circ\text{C}$  for 2 hours to obtain a transparent precursor solution.

The precursor solution is spin-coated on a  $10 \times 10 \text{ mm}^2$  LNO/STO substrate and rotated at a high speed of 5000 rpm for 30 seconds. On the hot table, the water in the film was removed by heating at  $120 \text{ }^\circ\text{C}$  for 3 minutes, and the organic solvent was removed by heating at  $300 \text{ }^\circ\text{C}$  for 3 minutes. Subsequently, the LAO sample was subjected to annealing in a hostler furnace at  $1050 \text{ }^\circ\text{C}$  for approximately 20 minutes.

**YMnO<sub>3</sub>.** The required amount of Yttrium nitrate hexahydrate ( $\text{Y}(\text{NO}_3)_3 \cdot 6\text{H}_2\text{O}$ , Macklin, 99.9%) and Manganese acetate ( $(\text{CH}_3\text{COO})_2\text{Mn}$ , Alfa, 98%) is dissolved in acetic acid, then 2, 4-pentanedione is added. A solution with a metal ion concentration of 0.2 mol/L is obtained, in which the ratio of acetic acid to 2, 4-pentanedione is 3:2. Finally, the mixed solvent was heated on a hot table at  $75 \text{ }^\circ\text{C}$  for 2 hours to obtain a transparent brown green precursor solution.

The precursor solution is spin-coated on a  $10 \times 10 \text{ mm}^2$  LNO/STO substrate and rotated at a high speed of 5000 rpm for 30 seconds. On the hot table, the water in the film was removed by heating at  $120 \text{ }^\circ\text{C}$  for 3 minutes, and the organic solvent was removed by heating at  $300 \text{ }^\circ\text{C}$  for 3 minutes. Subsequently, the YMO sample was subjected to annealing in a hostler furnace  $800 \text{ }^\circ\text{C}$  for approximately 20 minutes.

**BiFeO<sub>3</sub>.** The chemicals used in the experiment were bismuth oxide ( $\text{Bi}_2\text{O}_3$ , 99.9%, Aladdin) and iron oxide ( $\text{Fe}_2\text{O}_3$ , 99.9%, Aladdin). Polyvinyl alcohol was used as the binder for the target. The prepared target was sintered at  $750 \text{ }^\circ\text{C}$  for 2 hours. BFO films were fabricated by radio-frequency (RF) magnetron sputtering (VJC-300, Beijing VNANO Vacuum Technology Co., Ltd) on an LNO/STO substrate, which was heated at  $500 \text{ }^\circ\text{C}$ , and the cavity was vacuumized below  $2 \times 10^{-5}$  Torr. A total of 5.5 sccm of a mixture of nitrogen (45.5%) and oxygen (54.5%) was pumped into the chamber to maintain a pressure of 0.4 Pa. Continuous 2.5 hours of high RF power (90 W) sputtering and 0.5 hours of low RF (60 W) sputtering were performed. Finally, they were annealed under a full oxygen atmosphere for 20 minutes.

**Description of electrical stripping.** Using a 304 stainless steel clip, it can grasp a corner of the LAO, YMO, BFO, PZO, or STO film. This clip is affixed to the anode of the current source. Subsequently, the cathode of the current source is then connected to the carbon rod, which should then be immersed in an acetic acid solution. The applied current is 5 amperes, with the voltage of 10–25 V for LAO, YMO, PZO, and STO films and 1 V for BFO film. Acetic acid solution (10%) was selected as the dissolution solution, and the decomposition time was tested at the range of 0.1 A and the voltage with 0.1 V, 2 V, 5 V, 10 V, and 25 V, respectively. The voltage thresholds of different target layers may be related to their insulation properties, such as 25 V for PZO and 5 V for BFO. We have presented all the materials described in the manuscript, as well as some of the resistance values of the prospective materials for reference (Supplementary Table 2). The voltage threshold of the LNO sacrificial layer of 2 nm is determined to be between 10 and 100 pV.

Although a small amount of the  $[\text{La}(\text{CH}_3\text{COO})_n]^{3-n}$  complex products might be produced, it will quickly dissolve in the aqueous solution<sup>44</sup>. This will not have any impact on the target layer, and our characterization of the structure and electrical properties also confirms this point. The schematic diagram (Fig. 1d and 1e, Supplementary Figs. 1 and 10) of LNO sacrificial layer decomposition based on directional electrodynamic decomposition technology was drawn using *Microsoft Powerpoint* software.

## Characterization methods

**Density Functional Theory Calculations.** In the Density Functional Theory (DFT) calculations of the interface between the acetic acid and sacrificial layer, the projector augmented wave (PAW) method<sup>45</sup> as implemented in the Vienna Ab initio Simulation Package (VASP)<sup>46</sup> was employed. The Perdew-Burke-Ernzerhof (PBE) formulation was used for the exchange-correlation interactions. The calculations were performed in a spin-polarized manner. The cut-off energy of the plane-wave basis is set at 520 eV and the Brillouin zone integration was performed on a  $2 \times 2 \times 1$  *k*-points grid. The geometry structures were relaxed with a force threshold of 0.02 eV/Å. The unit cell of  $\text{LaNiO}_3$  is expanded by a factor of  $4 \times 4 \times 2$ , the 110 surface is cleaved, and a surface model is constructed with La as the terminal. The adsorption energy is calculated by subtracting the energies of the surface and the adsorbate from the energy of the adsorbed state.

Molecular Dynamic Simulation (MD) selected Materials Studio 2019 (Forcite module) to simulate A droplet with A diameter of 15 Å under 0 and 0.5 eV/Å/e electric fields in the NVT ensemble (Berendsen). Affinity behavior on LNO ( $13 \times 13 \times 4$ ) interface. And the affinity behavior of droplets forming channels in the center. Figure 3d presents the corresponding results and was drawn using the same software. Bader charge analysis is a charge occupancy analysis method based on quantum chemical calculations. Its core lies in determining the charge distribution of atoms in molecules or crystals through theoretical calculations (such as DFT). Essentially, it is the result of theoretical simulation rather than a physical quantity directly measured through experiments.

For finite element analysis, we used the solid-flow coupling method and COMSOL Multiphysics (6.3) software to deeply analyze the effects of liquid diffusion velocity and decomposition velocity on the stress of the target layer. Under the target layer with a thickness of 100 nm, the decomposition channels with a thickness of 5 nm and 20 nm were constructed, respectively, and the total length of the channels was set to 500 nm. By adjusting the inlet and outlet velocity of laminar flow, the change of diffusion velocity and decomposition velocity of different liquids was simulated. The simulation time was 4.65 s. In the process of model construction, the free triangle refinement mesh is used to divide the model to ensure the accuracy of the simulation results. In the simulation process, we used both the laminar flow module and the solid mechanics module. The density of the target

layer material is assumed to be  $1000 \text{ kg/m}^3$ , Poisson's ratio is 0.4, and Young's modulus is 1 MPa. The density and dynamic viscosity of the flowing liquid are  $1000 \text{ kg/m}^3$  and  $1 \text{ Pa}\cdot\text{s}$ , respectively. Finally, the transient solver MUMPS was used to solve the model to obtain detailed simulation data and provide strong support for the subsequent stress analysis. Figure 3e presents the corresponding results and was drawn using the same software.

**Current vs. time curve.** An electrochemical workstation (Shanghai Chenhua Instrument Co., LTD.) was used to test the electrochemical decomposition process of LNO.

**X-ray related diffraction.** The structure and orientation of the thin films were investigated via synchrotron XRD, XRR, and RSM measurements, which were conducted at the Diffuse X-ray Scattering Station of the Beijing Synchrotron Radiation Facility (BSRF), Beamline IW1A.

The thickness of the thin film can be determined by the angular distance of two consecutive maxima in XRR. And the thinner the thin film, the larger the oscillation period. We have roughly calculated the thickness of the thin film according to Equation:  $d = \lambda/2\Delta\theta$  where  $d$  is the thickness of the thin film,  $\lambda$  is the X-ray wavelength and  $\lambda = 1.5466 \text{ \AA}$ ,  $\Delta\theta$  is the period of the XRR stripes. XRR is usually correlated with the surface flatness and roughness of the film, so XRR can also prove that the film has a high-quality surface.

**UV spectra.** The ultraviolet-visible absorption spectra of the LNO sacrificial layer were measured with a UV-Vis T10 spectrophotometer.

**Optical photograph.** The sample that was transferred was examined using a three-ocular monocular metallographic microscope (Cb-15100).

**Ferroelectric hysteresis loop.** For macroscopic ferroelectric measurements, circular top Pt electrodes with a diameter of  $50 \mu\text{m}$  and a thickness of about  $20 \text{ nm}$  were deposited by magnetron sputtering. The ferroelectric hysteresis loops of the films were studied using TF-Analyzer 3000 (aixACCT).

**Transmission electron microscope.** TEM experiments were performed with FEI Titan Themis Cubed G2 300 (Cs Probe) TEM at  $300 \text{ kV}$ . The noise in the HAADF-STEM images was reduced by using a Gaussian Filter in the Velox software.

**Piezoresponse force microscopy.** The piezoresponse force microscopy (PFM) is performed by Asylum Research MFP-3D-Infinity with Olympus AC240TM Pt/Ti coated silicon cantilevers (Asylum Research, USA).

**Second harmonic generation.** The incident laser beam for the second harmonic generation (SHG) measurements was generated by a Spectra Physics Maitai SP Ti: Sapphire oscillator whose central wavelength is  $800 \text{ nm}$  and repetition frequency is  $82 \text{ MHz}$ . The incident power was fixed at  $50 \text{ mW}$  and focused on the sample surface with a diameter of  $\sim 100 \mu\text{m}$ . The  $p$ -out configurations were adopted during measurement, which denote the arrangements where the analyzer polarization is parallel to the plane of the incident light field. The polarization direction  $\phi$  of the incident light field is adjusted by the rotation of the  $\lambda/2$  waveplate driven by a rotating motor. The SHG intensity ( $I$ ) is related to the light-induced nonlinear polarization ( $P$ ) in the following way:  $I \propto |P|^2$ <sup>14</sup>.

**Piezoelectric sensor test.** A linear motor is used as a tool to adjust the curvature. The PZO and PDMS films are horizontally fixed on the fixed end of the linear motor. One end of the two copper wires is connected

to the two Pt electrodes, and the other end is connected to the positive and negative electrodes of the digital signal collector, respectively (Keithley 6514, Tektronix/Fortive), which is used to read the voltage signal generated when the PZO film is bent. The distance between the fixed end and the moving end of the linear motor is adjusted to make the film produce different bending angles, and the voltage signal of PZO film at different bending angles is obtained through the periodic movement of the linear motor.

## Data availability

All data needed to evaluate the conclusions in this study are available within the paper and its supplementary information files, or available from the corresponding author request.

## References

1. Dong, G. et al. Super-elastic ferroelectric single-crystal membrane with continuous electric dipole rotation. *Science* **366**, 475–479 (2019).
2. Huang, J.-K. et al. High- $\kappa$  perovskite membranes as insulators for two-dimensional transistors. *Nature* **605**, 262–267 (2022).
3. Sánchez-Santolino, G. et al. A 2D ferroelectric vortex pattern in twisted  $\text{BaTiO}_3$  freestanding layers. *Nature* **626**, 529–534 (2024).
4. Zhang, J. et al. Super-tetragonal  $\text{Sr}_4\text{Al}_2\text{O}_7$  as a sacrificial layer for high-integrity freestanding oxide membranes. *Science* **383**, 388–394 (2024).
5. Ji, D. et al. Freestanding crystalline oxide perovskites down to the monolayer limit. *Nature* **570**, 87–90 (2019).
6. Eom, K. et al. Electronically reconfigurable complex oxide heterostructure freestanding membranes. *Sci. Adv.* **7**, eabh1284 (2021).
7. Lee, D. et al. Heterogeneous integration of single-crystalline rutile nanomembranes with steep phase transition on silicon substrates. *Nat. Commun.* **12**, 5019 (2021).
8. Chen, S. et al. Braiding lateral morphotropic grain boundaries in homogenetic oxides. *Adv. Mater.* **35**, 2206961 (2023).
9. Xu, R., Huang, J., Barnard, E., Hong, S., Singh, P., Wong, E., Jansen, T., Harbola, V., Xiao, J., Wang, B., Crossley, S., Lu, D., Liu, S. & Hwang, H. Strain-induced room-temperature ferroelectricity in  $\text{SrTiO}_3$  membranes. *Nat. Commun.* **11**, 3141 (2020).
10. Guo, Y. et al. Remarkable flexibility in freestanding single crystalline antiferroelectric  $\text{PbZrO}_3$  membranes. *Nat. Commun.* **15**, 4414 (2024).
11. Bakaul, S. et al. Freestanding ferroelectric bubble domains. *Adv. Mater.* **33**, 2105432 (2021).
12. Zhong, H. et al. Large-scale  $\text{Hf}_{0.5}\text{Zr}_{0.5}\text{O}_2$  membranes with robust ferroelectricity. *Adv. Mater.* **34**, 2109889 (2022).
13. Yan, S. et al. Superconductivity in freestanding infinite-layer nickelate membranes. *Adv. Mater.* **7**, 2402916 (2024).
14. Xu, S. et al. Magnetoelectric coupling in multiferroics probed by optical second harmonic generation. *Nat. Commun.* **14**, 2274 (2023).
15. Kum, H. et al. Heterogeneous integration of single crystalline complex-oxide membranes. *Nature* **578**, 75–81 (2020).
16. Hong, S. et al. Extreme tensile strain states in  $\text{La}_{0.7}\text{Ca}_{0.3}\text{MnO}_3$  membranes. *Science* **368**, 71–76 (2020).
17. Lu, Z. et al. Cooperative control of perpendicular magnetic anisotropy via crystal structure and orientation in freestanding  $\text{SrRuO}_3$  membranes. *npj Flex. Electron.* **6**, 9 (2022).
18. Bourlier, Y. et al. Transfer of epitaxial  $\text{SrTiO}_3$  nanothick layers using water-soluble sacrificial perovskite oxides. *ACS Appl. Mater. Inter.* **12**, 8466–8474 (2020).
19. Zhang, Y. et al. Flexible quasi-two-dimensional  $\text{CoFe}_2\text{O}_4$  epitaxial thin films for continuous strain tuning of magnetic properties. *ACS Nano* **11**, 8002–8009 (2017).
20. Ma, H. et al. Wafer-scale freestanding vanadium dioxide film. *Sci. Adv.* **7**, eabk3438 (2021).

21. Chang, Y. et al. A fast route towards freestanding single crystalline oxide thin films by using  $\text{YBa}_2\text{Cu}_3\text{O}_{7-x}$  as a sacrificial layer. *Nanoscale Res. Lett.* **15**, 172 (2020).
22. Lu, D. et al. Synthesis of freestanding single-crystal perovskite films and heterostructures by etching of sacrificial water-soluble layers. *Nat. Mater.* **15**, 1255–1260 (2016).
23. Nian, L. et al.  $\text{Sr}_4\text{Al}_2\text{O}_7$ : A new sacrificial layer with high water dissolution rate for the synthesis of freestanding oxide membranes. *Adv. Mater.* **36**, 2307682 (2024).
24. Cai, S. et al. Enhanced polarization and abnormal flexural deformation in bent freestanding perovskite oxides. *Nat. Commun.* **13**, 5116 (2022).
25. Bakaul, S. et al. Single crystal functional oxides on silicon. *Nat. Commun.* **7**, 10547 (2016).
26. Paskiewicz, D., Sichel-Tissot, R., Karapetrova, E., Stan, L. & Fong, D. Single-crystalline  $\text{SrRuO}_3$  nanomembranes: A platform for flexible oxide electronics. *Nano Lett.* **16**, 534–542 (2016).
27. Yang, Q. et al. Capillary condensation under atomic-scale confinement. *Nature* **588**, 250–253 (2020).
28. Li, P., Huang, X. & Zhao, Y.-P. Electro-capillary peeling of thin films. *Nat. Commun.* **14**, 6150 (2023).
29. G., A. The modern theory and practice of pumping: a treatise on the application of the reynolds-stanton law of viscous flow to modern pumping problems and the flow of liquids through pipes. *Nature* **114**, 240 (1924).
30. Duggal, R., Hussain, F. & Pasquali, M. Self-assembly of single-walled carbon nanotubes into a sheet by drop drying. *Adv. Mat.* **18**, 29–34 (2006).
31. Yang, Q. et al. Ferroelectricity in layered bismuth oxide down to 1 nanometer. *Science* **379**, 1218–1224 (2023).
32. Xi, G. et al. Anionic strategy-modulated magnetic ordering in super-elongated multiferroic epitaxial films. *Nat. Commun.* **16**, 3526 (2025).
33. Tu, J. et al. Strain-controlled oxygen vacancy for robust ferroelectric  $\text{BiSmFe}_2\text{O}_{6.5}$  double-perovskite epitaxial thin films. *Appl. Phys. Rev.* **11**, 011413 (2024).
34. Tu, J. et al. Giant switchable ferroelectric photovoltage in double-perovskite epitaxial films through chemical negative strain. *Sci. Adv.* **11**, eads4925 (2025).
35. Yu, Z. et al. Room-temperature stabilizing strongly competing ferroelectric and antiferroelectric phases in  $\text{PbZrO}_3$  by strain-mediated phase separation. *Nat. Commun.* **15**, 3438 (2024).
36. Tu, J. et al. Atomical-rippled-nanodomains stabilized large polarization in  $\text{BiSmCo}_2\text{O}_6$  double-perovskite films. *Adv. Mater.* **e09635** <https://doi.org/10.1002/adma.202509635> (2025).
37. Burkovsky, R. G. et al. Field-induced heterophase state in  $\text{PbZrO}_3$  thin films. *Phys. Rev. B* **105**, 125409 (2022).
38. Zhang, Y. et al. Artificial ferroelectric-like hysteresis in antiferroelectrics with non-uniform disorder. *Acta Mater.* **294**, 121085 (2025).
39. Jiang, R.-J. et al. Atomic insight into the successive antiferroelectric–ferroelectric phase transition in antiferroelectric oxides. *Nano Lett.* **23**, 1522–1529 (2023).
40. Wu, C.-M., Chou, M.-H. & Zeng, W.-Y. Piezoelectric response of aligned electrospun polyvinylidene fluoride/carbon nanotube nanofibrous membranes. *Nanomaterials* **8**, 420 (2018).
41. Nguyen, M. D., Houwman, E. P. & Rijnders, G. Large piezoelectric strain with ultra-low strain hysteresis in highly c-axis oriented  $\text{Pb}(\text{Zr}_{0.52}\text{Ti}_{0.48})\text{O}_3$  films with columnar growth on amorphous glass substrates. *Sci. Rep.* **7**, 12915 (2017).
42. Nguyen, M. D. et al. Misfit strain dependence of ferroelectric and piezoelectric properties of clamped (001) epitaxial  $\text{Pb}(\text{Zr}_{0.52}\text{Ti}_{0.48})\text{O}_3$  thin films. *Appl. Phys. Lett.* **99**, 252904 (2011).
43. Tu, J. et al. Controllable chemical composition in double-perovskite  $\text{Bi}_{0.5}\text{Sm}_{0.5}\text{FeO}_3$  epitaxial thin films for ferroelectric, photovoltaic, and ferromagnetic properties. *Chem. Eng. J.* **453**, 139726 (2023).
44. Deberdt, S., Castet, S., Dandurand, J.-L., Harrichoury, J.-C. & Louisset, I. Experimental study of  $\text{La}(\text{OH})_3$  and  $\text{Gd}(\text{OH})_3$  solubilities (25 to 150 °C), and La-acetate complexing (25 to 80 °C). *Chem. Geol.* **151**, 349–372 (1998).
45. Kresse, G. & Joubert, D. From ultrasoft pseudopotentials to the projector augmented-wave method. *Phys. Rev. B* **59**, 1758 (1999).
46. Perdew, J. P., Burke, K. & Ernzerhof, M. Generalized gradient approximation made simple. *Phys. Rev. Lett.* **77**, 3865 (1996).

## Acknowledgements

This research was supported by the National Key R&D Program of China (2025YFA1411900, Zhang), the National Natural Science Foundation of China (22371013, Zhang and 22090042, Xing), the Fundamental Research Funds for the Central Universities (FRF-TP-19-055A2Z, Zhang), the National Program for Support of Top-notch Young Professionals, and the Young Elite Scientists Sponsorship Program by CAST (2019-2021QNRC, Zhang), the “Xiaomi Young Scholar” Funding Project (Zhang). We thank the Beijing Synchrotron Radiation Facility of 1W1A Beamline (<https://cstr.cn/31109.02.BSRF.1W1A>) for providing technical support and assistance in XRD and RSM measurements. Technical and human support provided by DIPC Supercomputing Center is gratefully acknowledged.

## Author contributions

L.Z. and X.X. supervised the project. H.L., J.T., and L.Z. conceived of the idea. H.L., J.T., S.D., G.X., and C.L. contributed equally to this work. H.L., J.T., S.D., E.S., and G.X. fabricated the epitaxial films and freestanding membranes and performed physical property characterizations. H.L. and Y.-W.F. performed the calculations and interpreted the data. D.Z. prepared lamellas for the STEM investigation. C.L. and X.Z. did the STEM characterization. S.X. and K.J. performed and analyzed the SHG measurements. J.T., X.-D.L., L.S., and X.-Q.L. conducted structure characterizations (XRD and RSM). H.L., J.T., L.G., S.O., J.-H.Z., J.-J.T., and L.Z. designed the research and analyzed the data. H.L., J.T., and L.Z. wrote the manuscript. All authors were involved in the data analyses and commented on the manuscript.

## Competing interests

The authors declare no competing interests.

## Additional information

**Supplementary information** The online version contains supplementary material available at <https://doi.org/10.1038/s41467-025-66697-6>.

**Correspondence** and requests for materials should be addressed to Linxing Zhang or Xianran Xing.

**Peer review information** *Nature Communications* thanks Betül Akkopru-Akgun and the other anonymous reviewer(s) for their contribution to the peer review of this work. A peer review file is available.

**Reprints and permissions information** is available at <http://www.nature.com/reprints>

**Publisher’s note** Springer Nature remains neutral with regard to jurisdictional claims in published maps and institutional affiliations.

**Open Access** This article is licensed under a Creative Commons Attribution-NonCommercial-NoDerivatives 4.0 International License, which permits any non-commercial use, sharing, distribution and reproduction in any medium or format, as long as you give appropriate credit to the original author(s) and the source, provide a link to the Creative Commons licence, and indicate if you modified the licensed material. You do not have permission under this licence to share adapted material derived from this article or parts of it. The images or other third party material in this article are included in the article's Creative Commons licence, unless indicated otherwise in a credit line to the material. If material is not included in the article's Creative Commons licence and your intended use is not permitted by statutory regulation or exceeds the permitted use, you will need to obtain permission directly from the copyright holder. To view a copy of this licence, visit <http://creativecommons.org/licenses/by-nc-nd/4.0/>.

© The Author(s) 2025

---

<sup>1</sup>Institute for Advanced Materials Technology, University of Science and Technology Beijing, Beijing, China. <sup>2</sup>State Key Laboratory of New Ceramics and Fine Processing, School of Materials Science and Engineering, Tsinghua University, Beijing, China. <sup>3</sup>State Key Laboratory of Radio Frequency Heterogeneous Integration (Shenzhen University), College of Electronics and Information Engineering, Shenzhen University, Shenzhen, China. <sup>4</sup>Physical Science and Engineering Division, King Abdullah University of Science and Technology (KAUST), Thuwal, Saudi Arabia. <sup>5</sup>Centro de Física de Materiales (CSIC-UPV/EHU), Donostia/San Sebastián, Spain. <sup>6</sup>Beijing National Laboratory for Condensed Matter Physics, Institute of Physics, Chinese Academy of Sciences, Beijing, China. <sup>7</sup>Electronic-Photonic Smart Sensing Device R&D Team, Inner Mongolia Key Laboratory of Intelligent Communication and Sensing and Signal Processing, School of Electronic Information Engineering, Inner Mongolia University, Hohhot, China. <sup>8</sup>School of Mathematics and Physics, University of Science and Technology Beijing, Beijing, China. <sup>9</sup>Guangdong Provincial Key Laboratory of Nanhai Microbial Mineralization Technology and Application, Guangzhou Maritime University, Guangzhou, China. <sup>10</sup>State Key Laboratory of Advanced Metallurgy, University of Science and Technology Beijing, Beijing, China. <sup>11</sup>Institute of Solid State Chemistry, University of Science and Technology Beijing, Beijing, China. <sup>12</sup>These authors contributed equally: Hangren Li, Jie Tu, Siyuan Du, Guoqiang Xi, Chen Liu. ✉e-mail: [linxingzhang@ustb.edu.cn](mailto:linxingzhang@ustb.edu.cn); [xing@ustb.edu.cn](mailto:xing@ustb.edu.cn)